Chains of magnetosomes with controlled endotoxin release and partial tumor occupation induce full destruction of intracranial U87-Luc glioma in mice under the application of an alternating magnetic field

Edouard Alphandéry, Ahmed Idbaih, Clovis Adam, Jean-Yves Delattre, Charlotte Schmitt, François Guyot, Imène Chebbi

▶ **To cite this version:**

1 **Chains of magnetosomes with controlled endotoxin release and partial**

2 **tumor occupation induce full destruction of intracranial U87-Luc glioma**

3 **in mice under the application of an alternating magnetic field.**

4 *Edouard Alphandéry [a,b,*], Ahmed Idbaih [c], Clovis Adam [d], Jean-Yves Delattre [c], Charlotte Schmitt [c],*

5 *François Guyot [a], Imène Chebbi [b].*

7 [a] Institut de minéralogie, de physique des matériaux et de cosmochimie, UMR 7590 CNRS, Sorbonne

8 Universités, UPMC, University Paris 06, Muséum National d'Histoire Naturelle, 4 Place Jussieu, 75005,

9 Paris, France.

10 [b] Nanobacterie SARL, 36 boulevard Flandrin, 75016, Paris, France.

11 [c] Inserm U 1127, CNRS UMR 7225, Sorbonne Universités, UPMC, University Paris 06, UMR S 1127,

12 Institut du Cerveau et de la Moelle épinière, ICM, F-75013, Paris, France.

13 AP-HP, Hôpitaux Universitaires Pitié Salpêtrière - Charles Foix, Service de Neurologie 2-Mazarin, F-

14 75013, Paris, France.

15 [d] Laboratoire de neuropathologie, GHU Paris-Sud-Hôpital Bicêtre, 78 rue du Général Leclerc, 94270 Le

16 Kremlin Bicêtre, France.

18 *Corresponding author Email address:

19 edouardalphandery@hotmail.com

ABSTRACT

Previous studies have shown that magnetic hyperthermia could efficiently destroy tumors both preclinically and clinically, especially glioma. However, antitumor efficacy remained suboptimal and therefore required further improvements. Here, we introduce a new type of nanoparticle synthesized by magnetotactic bacteria called magnetosomes with improved properties compared with commonly used chemically synthesized nanoparticles. Indeed, mice bearing intracranial U87-Luc glioma tumors injected with 13 µg of nanoparticles per mm^3 of tumor followed by 12 to 15 of 30 minutes alternating magnetic field application displayed either full tumor disappearance (40% of mice) or no tumor regression using magnetosomes or chemically synthesized nanoparticles, respectively. Magnetosome superior antitumor activity could be explained both by the increased production of heat and by endotoxin release under the alternating magnetic field application. Most interestingly, this behavior was observed when magnetosomes occupied only 10% of the tumor volume, which suggests that an indirect mechanism, such as an immune activity, is involved in tumor regression. This is desired for the treatment of infiltrating tumors, such as glioma, for which whole tumor coverage by nanoparticles can hardly be achieved.

KEYWORDS

Magnetosomes, magnetotactic bacteria, magnetic hyperthermia, alternating magnetic field, glioblastoma.

1. INTRODUCTION

A series of different nanotechnologies, such as lipid-based nanoformulations, polymer-drug conjugates, recombinant viruses, metallic nanoparticles, drug-targeted antibodies, and herbal nanoparticles, have been successfully developed for cancer treatment both at fundamental and industrial levels (1). Among them, technologies in which nanoparticle anti-tumor activity can be controlled by applying an external source of energy, such as a laser (2), (3), radiation (4), (5), ultrasound (6), (7), or magnetic field (8), (9) appear promising because they can potentially enhance both treatment safety and efficacy. Strategies to increase nanoparticle SAR by combining magnetic hyperthermia with photothermia using magneto-plasmonic nanohybrids have also been suggested (10), (11). There is interest in developing this type of nanotechnology for glioblastoma (GBM) treatment, especially for the most severe GBM cases, which are non-operable. With the current standard of care, *i.e.,* maximal safe surgery, concurrent radiochemotherapy and adjuvant chemotherapy, GBM, which affects 25,000 patients per year in the United States and Europe (12), (13), remains incurable with a poor prognosis. The five-year survival time of patients with GBM is low at 10% (14), (15), demonstrating the need for new treatment options (16), (17), (18), (19), (20). Among the potential treatments for GBM are different types of nanothermotherapies (21), such as photodynamic therapy (22) and magnetic hyperthermia, which have been tested to treat GBM (9). Compared with other thermotherapies, magnetic hyperthermia (23), (24), (25), (26), (27), in which tumors are typically heated to 43-50 °C by intratumor administration of iron oxide nanoparticles followed by alternating magnetic field (AMF) application, appears promising. This is due to more localized heat produced by the nanoparticles, which results in enhanced efficacy, and to tumor destruction achieved at lower temperatures, which strengthens treatment safety. In a clinical trial that enrolled 14 patients with GBM, magnetic hyperthermia treatment performed using small chemically synthesized iron oxide nanoparticles (IONP) was well-tolerated by

patients, did not produce major side effects, and led to an increased survival time of 7 months compared with conventional treatments (28), (29).

Treatment efficacy could potentially be further improved by using chains of magnetosomes (CM), which are iron oxide nanoparticles synthesized by magnetotactic bacteria, instead of IONP. In previous studies, CMs have been shown to destroy MDA-MB-231 breast tumors subcutaneously xenografted under the skin of mice more efficiently than IONPs (30), (31). Magnetosome efficacy was attributed to the large magnetosome size, leading to stable ferrimagnetic properties and to a large amount of heat produced under AMF application, as well as to an arrangement of chains that prevented aggregation and promoted homogenous magnetosome distribution in the tumor (32), (33), (34), (35).

In the present study, anti-tumor activity against U-87-Luc GBM was studied both *in vitro* and *in vivo* with a suspension containing CMs. We first demonstrated that the amount of endotoxins released from the CMs can be controlled under AMF applications. CM cytotoxicity and internalization properties in the presence of U87-Luc cells were also studied *in vitro*. Mice bearing intracranial U87-Luc tumors were then treated under conditions that could be followed clinically, *i.e.,* using an AMF with 30 mT and 198 kHz (H.f = 8 10^8 A.m^{-1}.s^{-1}, below the threshold of 5.10^9 A.m^{-1}.s^{-1}, above which Eddy currents may occur) (26),(36). Treatment parameters, such as the number of magnetic sessions and quantity of CMs administered, that lead to complete disappearance of the intracranial U87-Luc tumors were determined and compared with IONP treatment, which has been previously used to perform preclinical magnetic hyperthermia tumor treatments (37), (38). During the various treatments, nanoparticle distribution in the tumors and the presence of different cell types in the brain were also examined by histology. This study also suggests a mechanism for tumor destruction and verified that the brain tumor disappeared fully following magnetic hyperthermia treatment with CMs.

2. MATERIALS AND METHODS

2.1. Preparation of the injectable CM suspension

4

Magnetospirillum magneticum AMB-1 magnetotactic bacteria at biosafety level 1 were purchased from ATCC (79024 strain). Five milliliters of a suspension containing 4.10^6 of these bacteria per milliliter were introduced into one liter of sterile 1653 ATCC culture medium containing nutrients and additives, such as minerals, vitamins, and an iron source, as listed in the 1653 ATCC medium, which is required for the proliferation of these bacteria and for magnetosome production. The bottles were completely filled with sterile medium to prevent contamination by other bacterial species and to avoid a high oxygen concentration in the growth medium, which would prevent magnetosome production. The media containing the bacteria were then placed in an incubator at 30 °C for 7 days to enable bacterial growth and magnetosome production. After 7 days, the media was centrifuged at 4000 g for 45 minutes. The bacterial pellet was washed using 1 ml of sterile water (Millipore®). Magnetotactic bacteria were concentrated using a strong Neodinium magnet (0.6 Tesla), re-suspended in 0.05 M TRIS and sonicated with a sonicating finger at 0 °C for 2 hours at 30 W. The suspension containing the chains of magnetosomes extracted from the magnetotactic bacteria was washed several times with sterile water using a magnet to isolate the CMs from the supernatant containing cellular debris and residual bacteria until the cellular debris disappeared from the supernatant. Sonication was performed at 30 W by a series of three 2-second pulses between each wash. The CMs were then re-suspended in 1 ml of sterile water. For the intracranial injections, the CMs were re-suspended in a sterile injectable solution containing 5% glucose and exposed to ultraviolet lamp (UV) irradiation for 12 h for partial sterilization.

2.2. Preparation of IONPs:

IONPs, which are starch-coated iron oxide nanoparticles, were purchased from Micromod Partikeltechnologie GmbH company, Friedrich-Barnewitz-Str. 4, D-18119, Rostock, Germany (ref: 10-00-102).

2.3. Nanoparticle Characterization:

Nanoparticle sizes, shapes, and organization were determined using a transmission electron microscope (JEM-2100, JEOL, Japan). The iron concentrations of the different nanoparticle suspensions were measured by mixing these suspensions with hydrochloric acid and hydrogen peroxide to produce Fe^{3+}

ions complexed with potassium thiocyanate, and total iron was then determined via an absorbance

measurement at 476 nm. The concentrations were expressed as mg of maghemite contained in the CMs

and IONPs per ml of suspension or per mm^3 of tumor. The zeta potentials of the different nanoparticles

in suspension were measured by dynamic light scattering (DLS, ZEN 3600, Malvern Instruments, UK).

The stability of the nanoparticle suspensions was estimated by measuring the changes in the optical

densities of these suspensions, which were measured at 476 nm for 15 min. Nanoparticle FTIR spectra

were recorded with a FTIR spectrometer (Vertex 70, Bruker, USA). The amount of organic material at

the nanoparticle surface was measured using an elemental CHNS analyzer (Flash EA 1112, Thermo

Fisher Scientific, USA). More details about each of these techniques are provided in the supplementary

materials section.

2.4. Set-up for generating the alternating magnetic field and for measuring the temperature

We used an induction system operating at 198 kHz to generate the alternating magnetic field. Mice,

Eppendorf tubes, petri dishes containing nanoparticles and possibly cells were inserted into a coil with a

7-cm diameter with four spires to generate a magnetic field with an average strength of 30 mT. We used

an infrared camera (EasIR-2, Optophase, France) positioned 20 cm above the coil to measure the

temperature both *in vitro* and *in vivo*. We verified the temperature with a thermocouple positioned at the

tumor center and that the infrared camera measured the temperature at the tumor center. This was

possible due to the shallowness of the tumor.

2.5. Amount of endotoxins released under AMF application

Suspensions containing 2 µl of CMs or IONPs at a concentration of 20 mg/ml in iron oxide were treated

as follows. Nanoparticle suspensions were exposed to 0, 1, 2, 3, and 4 magnetic sessions, during which

an AMF of 198 kHz and average strength of 30 mT was applied for 30 minutes. After AMF

applications, 100 µl of nonpyrogenic water was added to the suspensions, and the suspensions were

mixed for one minute and centrifuged at 13 000 rotations per minute for 15 minutes. The endotoxin

concentration of the supernatant was measured using the Limulus amebocyte lysate (LAL) assay.

2.6. Materials and cells culture

146 U87-MG Luc human GBM cell lines, which were transduced with a luciferase gene, were obtained from

147 Keith Ligon's lab and used in this study. After thawing, the U87-MG Luc adherent cells were cultivated

148 at 37 °C in the presence of 5% CO_2 in Dulbecco's Modified Eagle Medium (DMEM) containing 10%

149 fetal bovine serum (FBS). Once the cells reached confluence, the culture dishes were rinsed with Hank's

150 Balanced Salt Solution (HBSS). The cells were then detached with trypsinization for 5 minutes at 37 °C

151 in the presence of 5% CO_2. The trypsin activity was stopped by the addition of medium containing FBS.

152 The cellular concentration was then determined using a Malassez cell.

153 ### *2.7. U87-Luc cytotoxicity in the absence of AMF using an MTT assay*

154 U87-Luc cytotoxicity studies were evaluated using an MTT assay. This technique measures the ability of

155 mitochondrial enzymes to reduce 3-(4,5-dimethylthiazol-2-yl)-2,5-diphenyltetrazolium bromide to

156 purple formazan crystals. Cells were seeded at a density of 10^4 cells per well in 96-well flat-bottom

157 plates and incubated in completed culture medium for 24 h. Then, the U87-Luc cell medium was

158 removed and replaced with 10% FCS-medium containing CMs or IONPs at varying concentrations

159 ranging from 7.8 µg/ml to 1000 µg/ml in maghemite. After 24 h of incubation, the cells were washed

160 with HBSS and incubated with 0.1 ml of MTT (2 mg/ml) for an additional 4 h at 37 °C. The insoluble

161 product was then dissolved by the addition of 100 ml of isopropanol. The absorbance corresponding to

162 the solubilized formazan pellets, which reflect the relative viable cell numbers, was measured at 540 nm

163 using a microplate reader. We measured the absorbance at 540 nm for the cells with the nanoparticles

164 without formazan blue and we have subtracted this signal from the signal for the cells with nanoparticles

165 with formazan blue. The percent inhibition of cell proliferation, inhibition (%), was then estimated using

166 the following formula: % inhibition = $[1-(OD_{TC}/OD_{UC})] \times 100$, where OD_{UC} is the optical density of the

167 suspension of untreated cell, *i.e.,* cells that have been washed with PBS and have not been in the

168 presence of nanoparticles, measured at 540 nm, and OD_{TC} is the optical density of the suspension of

169 treated cells, *i.e.,* nanoparticle suspensions that have been added to cells, measured at 540 nm. The

170 percent inhibition of cell proliferation was plotted as a function of the nanoparticle concentration. The

171 experiments were performed in triplicate.

7

2.8. In vitro efficacy of hyperthermia

A total of 500,000 U87-Luc cells were seeded in a Petri dish (35 mm) for 24 hours. Then, 2 ml of IONP and CM suspensions were added to the cells at different concentrations varying between 1 mg/ml, which is sufficient to induce an increase in temperature increase, and 40 µg/ml, which corresponds to the maximum magnetosome concentration in the tumor, *i.e.*, 40 µg of magnetosomes per mm^3 of tumor. When the same amount of nanoparticles used, we observed an increase in the temperature in solution but not *in vitro*, possibly due to the lower concentrations *in vitro* (2 ml at 20 µg/ml) than in solution (2 µl at 20 mg/ml). Next, these assemblies were exposed (or not) to a 30 mT and 198 kHz AMF for 30 minutes. The cells were then incubated with the nanoparticles for 24 h. The nanoparticle media was removed, and the cells were washed twice with cold PBS. We verified that there were no observable nanoparticle aggregates at the cell surface and that the nanoparticles were mostly internalized in cells by optical microcopy. It is possible that nanoparticles that were not observed with the optical microscope remained at cell surface, meaning that the measurement provides an estimate of the maximum quantity of internalized nanoparticles or the amount of nanoparticles internalized in cells or at the cell surface. Next, 250 µl of trypsin were added to detach the cells, and then the culture media was mixed with cells. Following this *in vitro* treatment, the mixtures were centrifuged at 800 rpm for 7 minutes. The supernatant was removed and replaced with 100 µl of annexin-binding buffer, 5 µl of Alexa Fluor 488 Annexin V for early apoptosis detection, and 1 µl of propidium iodide at 100 µg/ml for late apoptosis and necrosis detection. The mixtures were incubated at room temperature for 15 minutes. Then, 400 µl of annexin-binding buffer was added to this cell suspension and mixed gently. Ten microliters of this suspension were loaded into the sample slide and were inserted completely into a Countess™ II FL Automated Cell Counter (Thermo Fisher scientific), which was able to detect the Annexin and Propidium Iodide emissions. The percentages of necrotic and apoptotic cells were thus obtained.

2.9. Internalization of nanoparticles

Following the *in vitro* treatments described in 2.7, the different mixtures were loaded into the sample slide and completely inserted into a Countess™ II FL Automated Cell Counter to count the cells. The

mixtures were then centrifuged, and the supernatant was removed and replaced with 286 µl of HNO_3 (70%); the resulting treated mixtures were maintained at 4 °C for 24 h to lyse cells and dissolve the nanoparticles into free iron. Finally, 10 ml of filtered water was added to all the treated mixtures and the iron concentration was then determined using ICP-AES measurements. We deduced the average quantity of iron coming from the nanoparticles, which was internalized in each cell.

2.10. In vivo experiments

In vivo experiments were performed following ethical guidelines and surgery was performed following the guidelines of the Institutional Animal Care and Use Committee ("Ethic committee Charles Darwin N°5", project ethic number: 00764.03). Mice were fed and watered according to these guidelines and euthanized by cervical dislocation when their weights had decreased by more than 20% or when signs of pain, unusual posture or prostration were observed. At day 0 (D0), a cell suspension containing 10^5 U87-Luc cells per microliter was first inoculated into the brains of 7-week-old CD-1 female nude mice with a mean weight of 20 g from Charles River. To achieve the surgical procedure leading to cell implantation, the mice were first anesthetized with a mixture of ketamine (100 mg/kg) and xylazine (8 mg/kg). The mouse head was then fixed in a stereotactic frame, a craniotomy was performed at the fixed coordinates (0.2.0) and 2 µl of a suspension containing 2.10^5 U87-Luc cells were injected at the coordinates (0.2.2). Tumors grew for 8 days between D0 and D8. At D8, 7 different groups containing 10 mice each were treated as follows (Table S1(a)):

-        Group 1 received a 30 mm³ GBM at coordinates (0.2.2) mm and 2 µl of an isotonic solution containing 5% glucose without any further treatment;

-        Group 2 received a 5 mm³ GBM at coordinates (0.2.2) mm and the same glucose solution as Group 1, followed by magnetic treatment consisting in 12 magnetic sessions (S) on D8 (S1), D9 (S2), D10 (S3), D15 (S4), D16 (S5), D17 (S6), D22 (S7), D23 (S8), D24 (S9), D29 (S10), D30 (S11), and D31 (S12);

-        Group 3 received a 3 mm³ GBM at coordinates (0.2.2) mm and a suspension containing 40 µg of magnetosome chains in maghemite without any further treatment;

224 -   Group 4 received a 3 mm^3 GBM at coordinates (0.2.2) mm and the same suspension as Group 3,

225 followed by magnetic treatment consisting in 15 magnetic sessions on D8 (S1), D9 (S2), D10 (S3), D15

226 (S4), D16 (S5), D17 (S6), D22 (S7), D23 (S8), D24 (S9), D29 (S10), D30 (S11), D31 (S12), D36 (S13),

227 D37 (S14), and D38 (S15);

228 -   Group 5 received a 25 mm^3 GBM at coordinates (0.2.2) mm and the same suspension as group 3,

229 followed by 15 magnetic sessions on D8 (S1), D9 (S2), D10 (S3), D15 (S4), D16 (S5), D17 (S6), D22

230 (S7), D23 (S8), D24 (S9), D29 (S10), D30 (S11), D31 (S12), D36 (S13), D37 (S14), and D38 (S15);

231 -   Group 6 received a 5 mm^3 GBM at coordinates (0.2.2) mm and 40 µg of IONPs in maghemite

232 without any further treatment; and

233 -   Group 7 received in a 3 mm^3 GBM at coordinates (0.2.2) mm and the same suspension as Group

234 6, followed by 12 magnetic sessions on D8 (S1), D9 (S2), D10 (S3), D15 (S4), D16 (S5), D17 (S6), D22

235 (S7), D23 (S8), D24 (S9), D29 (S10), D30 (S11), and D31 (S12).

236 For the different groups of mice, the bioluminescence intensity emitted by the living tumor cells was

237 measured on D7, D14, D21, D28, D35, D42, D49, D56 and D150.

238 During each magnetic session (S1 to S15), the mice were exposed to an AMF at an average strength of

239 30 mT and a frequency of 198 kHz that was applied for 30 minutes.

240   *2.11.   Bioluminescence intensity and tumor volume measurements*

241 The mice were first anesthetized using isoflurane. The bioluminescence intensity was then measured

242 using an IVIS Spectrum *"In Vivo Imaging System"* (PerkinElmer, Inc.) 10 minutes after intraperitoneal

243 injection of 100 mg/kg of beetle luciferin potassium salt (Promega: E1605) in PBS, which reacts with

244 luciferase to produce luminescent oxo-luciferin, (39), (40), (41). Images were analyzed with the

245 living Image 4.0 software from Caliper, Life Sciences. The bioluminescence intensity at the tumor site

246 was divided by the bioluminescence intensity measured in the flanks to remove the mouse auto-

247 luminescence signal. Then, the relationship between tumor bioluminescence intensity and tumor volume

248 was determined. For that, bioluminescence intensities were measured at D7, D14, D21, D28 and D35 in

249 a series of living mice. The tumor volumes were deduced from surface measurements of several

horizontal histological sections positioned at various tumor heights, which were collected from mice euthanized on the same day at the BLI measurements. A linear relationship was observed between the logarithm of tumor bioluminescence intensity (BLI), log(BLI), and the logarithm of the tumor volume expressed in mm^3, log (volume(mm^3))(Fig. S3). A linear coefficient of 1.4 was deduced by fitting the plot in Fig. S3 with a linear function, a value that agrees with previously reported values (40), (42), (43), (44).

2.12.   *Representation of tumor volume variations and estimates of survival time*

The variations in tumor volume in time were represented in Tukey diagrams using the Kaleida Graph 4.03 software. Mouse survival times are plotted using the Kaplan-Meier model method (45), (46). The statistical significance of the survival time between the different groups was evaluated using the log rank test. Parameters are expressed as the median with p-values (9).

2.13.   *Temperature measurements*

Intratumor temperatures were measured as a function of time during the various treatments in living mice using an infrared camera (EasIRTM^{-2}, Optophase) placed 20 cm above the coil.

### 2.14.   *Histological analysis*

Histological studies were performed on extracted brains that were fixed with a 4% solution of formaldehyde for 24 hours, cut into 2-mm thickness transverse slices, washed in an ethanol (70%) bath for 12 hours and included in paraffin. Sections of paraffin blocks with a thickness of 4 μm were deposited on glass slides and stained with hematoxylin-eosin (H&E) and/or Prussian blue to distinguish between healthy and tumor areas and to determine the location of the magnetosomes, polynuclear neutrophils (PNN), and tumor and healthy cells. Histological analysis was also performed on the mice that received glucose on day 8 and were euthanized 6 or 24 hours following glucose injection (Figs. S5(a) and S5(c)). Six mice were analyzed at various times, including after 1 magnetic session (Figs. S5(b)) or 24 hours after 3 magnetic sessions (Fig. S5(d)), in which they received CM on day 8 and were euthanized 4 hours (Figs. 9(a) and 9(c)) or 72 hours (Figs. 9(b) and 9(d)) after the CM injection; just after or 4 hours after 1 magnetic session (Figs. 8(a), 8(b) and 8(c)); and 24 hours after 3 magnetic

11

276 sessions (=72 hours, Figs. 8(d) to 8(g)), in which they received IONPs on day 8 and were euthanized 6

277 or 72 hours after IONP administration (Figs. S4(a) and S4(c)) or 24 hours after 3 magnetic sessions (72

278 hours (Figs. S4(b) and S4(d)).

279 **3.   RESULTS AND DISCUSSION**

280   *3.1. Properties of CMs and IONPs used for the tumor magnetic hyperthermia treatments*

281 CMs were extracted from AMB-1 whole magnetotactic bacteria, a species of bacteria that produces

282 chains of nanoparticles called magnetosomes, as shown in the TEM image of a typical magnetotactic

283 bacterium presented in Figure 1(a). After extraction from the magnetotactic bacteria, the magnetosomes

284 maintain their organization in chains (Figure 1(b)), a type of organization that is advantageous for the

285 treatment because it prevents aggregation and promotes uniform distribution and homogenous heat

286 production. Magnetosomes appear to possess a cubooctahedric geometry, more uniform sizes and shapes

287 than IONPs (Figs. S7(a) and S7(b)), a size that is larger than 20 nm for the majority of them and a mean

288 size of ~45 nm (Fig. S1(a)), which leads to a coercivity H_c of ~200-300 Oe and a ratio between remnants

289 and saturating magnetization of Mr/Ms ~ 0.35 at physiological temperature (Fig. S6), (47).

290
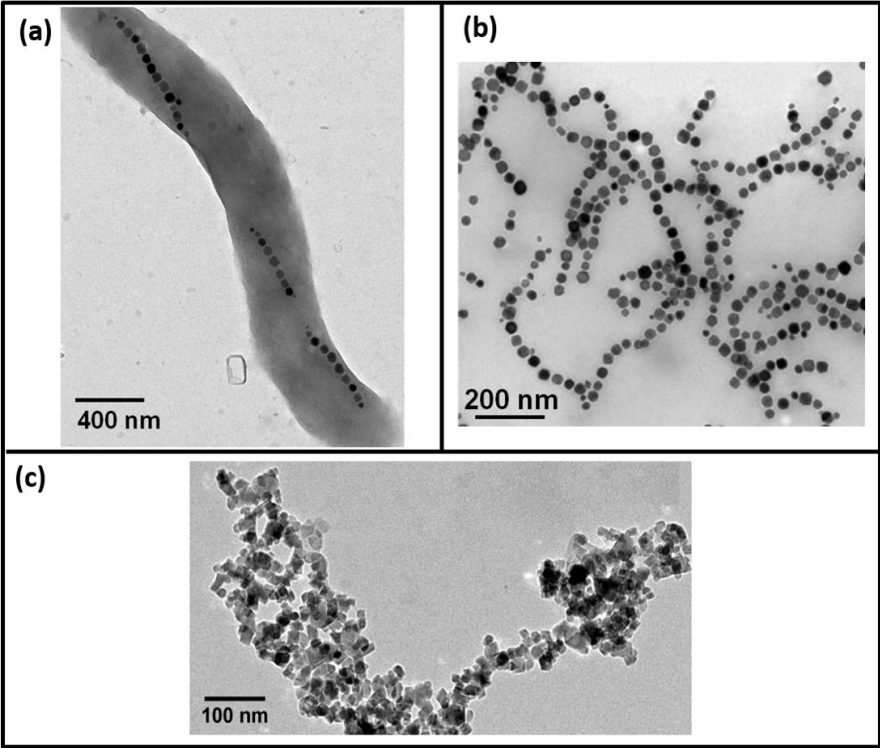
Figure 1: Transmission electron microscopy images of (a) an AMB-1 *Magnetospirillum magnetotacticum* magnetotactic bacterium, (b), chains of magnetosomes extracted from magnetotactic bacteria and (c) an IONP. Seven microliter suspensions containing magnetotactic bacteria, chains of magnetosomes, and IONPs were deposited and dried on top of a carbon grid before TEM observation.

Magnetosomes are composed of a core, which is made of iron oxide, as revealed by the FT-IR Fe-O peak at 580 cm^{-1} (table 1) and further determined to be maghemite by saturating isothermal remnant magnetic measurements (47). The core is surrounded by a coating of organic material, including phospholipids and lipopolysaccharides, as revealed by a series of FT-IR peaks [C=O at 1740 cm^{-1}, amide at 1650 cm^{-1}, amine at 1530 cm^{-1}, P=O at 1250 cm^{-1}, and PO at 1050 cm^{-1} (Table 1)]. The coating, whose function is to bind magnetosomes together in chains (48), is estimated to be 1 to 5 nm thick (Figure 1(b)) and to contain 13.9% carbon, as estimated by CHNS analysis. LAL measurements further indicated that the organic material at the magnetosome surface is partially derived from endotoxins whose concentration in CM suspensions is estimated as 1400-8400 EU per ml per mg of iron oxide. Moreover, CM suspensions appear sufficiently stable to enable their *in vivo* administration, as their absorption measured at 480 nm does not decrease by more than 30% within 20 minutes (Table 1).

	CM						IONP					
Endotoxin level (EU/mg/mL)	1400-8400						< 50					
% stability on water (iron concentration = 1mg/mL)	70						100					
Coating thickness (nm)	1 - 5						1					
Isoelectric Point (a.u)	4.2						9.5					
pH	2	4	6	8	10	12	2	4	6	8	10	12
ζ-Potential (mV)	20	2.5	- 18	- 26	-34	- 38	7	6	6	5	3	- 20
% C	13.9						8.7					
SAR (2μL, 40 μg of iron) (W/gFe)	Water			Brain			Water			Brain		
	57			4			10			0		
FT-IR (cm^{-1})	580	1050	1250	1530	1650	1740	610		1025		1150	
	Fe-O	P-O	P=O	N-H (amine)	N-H (amide)	C=O	Fe-O		C-O (alcohol)		C-O (ether)	

Table 1: The endotoxin content estimated in Endotoxin units (EU per mg in iron per ml), percent decreased absorption measured at 480 nm in suspensions containing CM and IONP at a concentration of 1 mg in iron per ml after twenty minutes, and estimates of the isoelectric point and zeta potential as a function of pH for suspensions containing CMs or IONPs.

Estimates of the coating thickness measured by transmission electron microscopy and percentage of carbon (% C) measured with CHNS and assignments from the different FT-IR peaks measured by FT-IR for the CM and IONP dried suspensions. Estimates of the specific absorption rates (SAR) in W per gram in iron for 2 µl containing 40 µg of CMs or IONPs in iron oxide mixed in water or introduced inside the mouse brains.

Compared with CMs, IONPs are also ferromagnetic iron oxide nanoparticles but characterized by the following distinct features. Their geometric structure is parallelepipedic, they are not organized in chains and tend to form small aggregates as observed in the TEM image in Figure 1(c). INOPs are made of a core measuring ~19 nm by TEM (49), and whose composition is iron oxide as determined by FT-IR measurements that display an Fe-O peak at 610 cm^{-1} (Table 1). The IONP core is surrounded by synthetic hydroxyethyl starch, as suggested by FT-IR and CHNS measurements performed on the IONPs, which shows FT-IR peaks at 1150 cm^{-1} and 1050 cm^{-1} that are attributed to hydroxyethyl starch ether and alcohol functional groups, and has a carbon percent of 8.7%, revealing the presence of an organic coating surrounding the inorganic iron oxide core (Table 1). Compared with CMs, the IONP surface contains a much lower endotoxin concentration of 50 EU per ml per mg of iron oxide, as measured with the LAL assay. Furthermore, IONPs are characterized by ferrimagnetic properties at physiological temperatures but at the following lower values: (1) H$_c$ ~ 120 Oe and (2) M$_r$/M$_s$ ~ 0.15 (49), (Fig. S6 and Table 1), which should yield lower SAR values. Furthermore, given that they are not less stable than CMs (Table 1) and that their anti-tumor efficacy has been demonstrated on tumor-bearing mice using magnetic hyperthermia (50), IONPs appear to be good standard for comparison to assess CM efficacy.

3.2. Under AMF applications, CM can release heat and an immune-stimulating substance more efficiently than IONPs

In an attempt to mimic the conditions in the *in vivo* treatments and to study the release of endotoxins from the CM and IONP surfaces in these conditions, we introduced 2 µl of suspensions containing 40 µg of these nanoparticles in iron oxide at the bottom of a tube that we exposed to 1, 2, 3, and 4 magnetic sessions during which an AMF of 198 kHz and average strength 30 mT was applied for 30 minutes. During each of these 4 magnetic sessions, CM and IONP suspensions led to maximal temperatures

14

337   (T_{max}) of 57 °C and 28 °C, respectively, after 3 minutes of AMF application (Fig. S2(a)). Specific

338   absorption rates (SAR) were deduced from the formula $SAR=C_{water}(\Delta T/\delta t)/C_m$, where $\Delta T/\delta t$ are the

339   initial slopes of the plot in Fig. S2(a) [$\Delta T/\delta t$ = 0.27 °C/sec and 0.05 °C/sec for CM and IONP,

340   respectively], C_{water}= 4.2 J/g.K is the specific heat capacity of water, and C_m = 0.02 g/mL is the

341   concentration in iron oxide of the different nanoparticle suspensions. The SARs were estimated as 57 ±

342   6 W/g_{Fe} and 10 ± 3 W/g_{Fe} for CMs and IONPs, respectively. Therefore, the heating properties of CMs
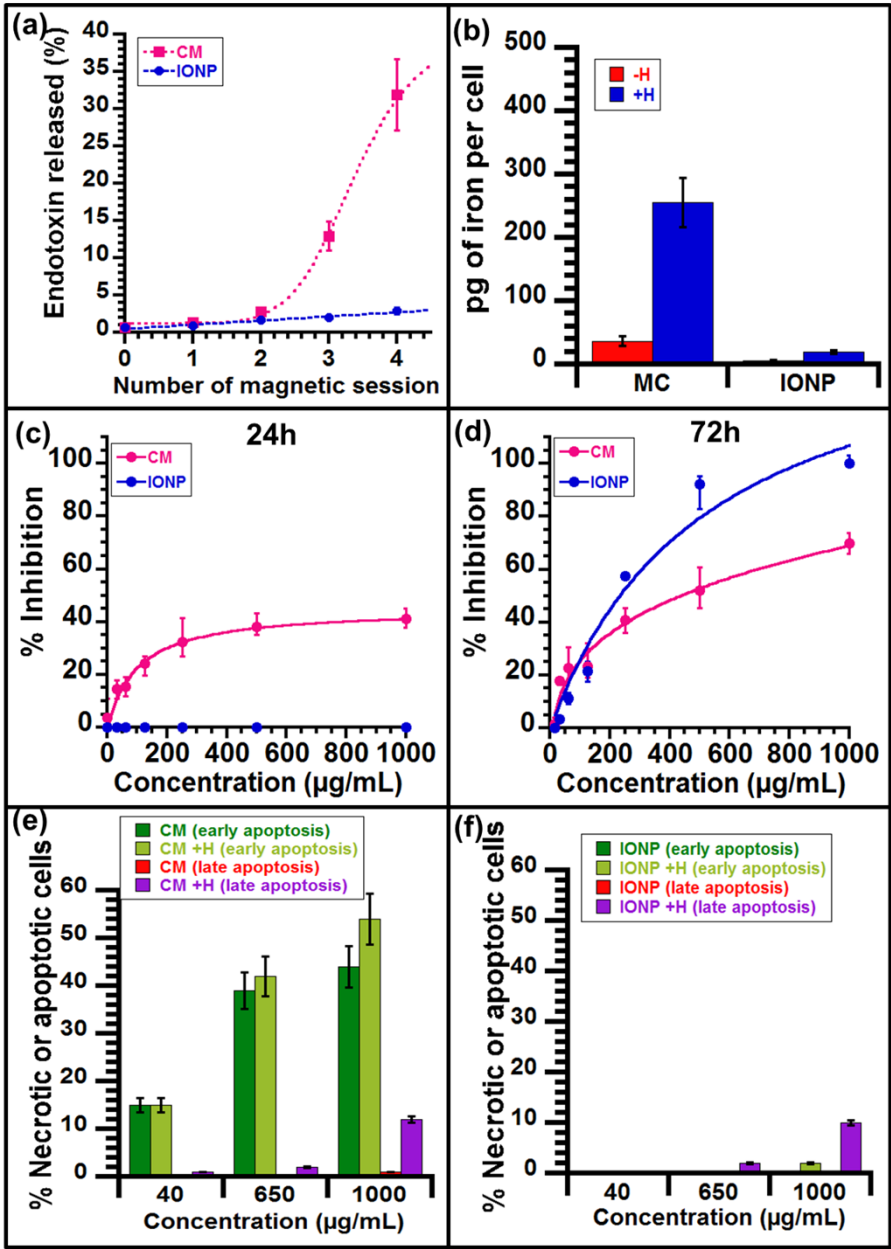
343   appear far superior to those measured for IONPs.

344

Figure 2: (a) Percentage of endotoxin release from 2 µl suspensions containing 40 µg of CM or IONP in iron oxide that were exposed to 1, 2, 3 or 4 S with an AMF of 198 kHz and average strength of 30 mT applied for 30 minutes. (b) The quantity of iron released from MCs and IONPs, measured in pg and internalized per cell from U87-Luc cells incubated for 24 hours with 1 mg/mL of CM or IONP in maghemite with(+H)/without(-H) AMF, where the AMF is the same as in (a). (c and d) The percentage inhibition of cell proliferation as a function of nanoparticle concentration for CMs and IONPs in maghemite in U87-Luc cells incubated for (c) 24 hours or (d) 72 hours with nanoparticle concentrations varied between 8 µg/mL and 1 mg/mL. (e and f) The percentages of late apoptotic (+ necrotic) and early apoptotic cell death as a function of nanoparticle concentration with(H)/without(-H) AMF where the AMF is the same as in (a) in U87-Luc cells incubated for 24 hours with (e) CM and (f) IONP at concentrations of 40 µg/mL, 650 µg/mL, and 1 mg/mL.

Moreover, the percentage of endotoxin release, which remains relatively similar at 1 to 3% during the first 2 magnetic sessions, strongly increased to 11% and 32% following the third and fourth magnetic sessions, respectively (Fig. 2(a)). This indicates that endotoxins, which are initially at the magnetosome surface, are progressively released from CMs under AMF application. Using CMs exposed to AMF, it therefore appears possible to simultaneously produce heat and release an immune-stimulating substance such as an endotoxin. Although endotoxins cannot be used in medicinal preparations, they may be replaced by a nontoxic equivalent, such as M-PLA, (51), (52). Combining the production of localized heat with the release of such a substance may possibly enhance antitumor efficacy. Compared with CMs, IONPs released a lower quantity of endotoxins and their percentage of endotoxin release did not exceed 5% between 1 and 4 S (Fig. 2(a)). Taken together, these heating and endotoxin release behaviors suggest that IONPs are less promising than CMs for the magnetic hyperthermia and endotoxin treatment in tumors.

3.3. CMs induce enhanced U87-Luc early apoptotic cell death and internalization in vitro

In the absence of the AMF, *the* cytotoxicity of CMs towards U87-Luc cells was compared with that of IONPs using nanoparticle suspensions that were added to the cells and incubated for 24 and 72 hours at concentrations between 40 µg/mL and 1 mg/mL. At 24 hours, the percent inhibition of cell proliferation increased with increasing nanoparticle concentrations from 0 to 40% for CM and remained at 0% for the IONPs (Figure 2(c)). At 72 hours, the percent inhibition increased more significantly for CMs, *i.e.,* from

0 to 60%, than for IONPs, *i.e.,* from 0 to 100% (Figure 2(d)). While CMs were observed to be more cytotoxic than IONPs at 24 hours, the opposite behavior was observed at 72 hours.

U-87-Luc cells were also incubated for 24 hours with CMs and IONPs at three different concentrations of 40, 650, and 1000 µg/ml and then exposed to an AMF of 198 kHz and strength 47 mT for the first 30 seconds and 30 mT for the remaining 29.5 minutes in an attempt to reach 41 °C, a temperature above which mild hyperthermia conditions are expected to occur （30）. The 40 and 650 µg/ml concentrations led to temperature increases of less than 2 °C, which were insufficient to reach the hyperthermia conditions. These concentrations resulted in necrosis and late apoptosis percentages that remained below ~ 4% with/without AFM for the CMs and IONPs and early apoptosis percentages that were similar with/without AFM at ~ 15% and ~ 40% for CMs at 40 and 650 µg/ml in iron oxide, respectively, and at 0% for IONPs (Figs. 2(e) and 2(f)). In contrast, at a concentration of 1 mg/ml, both CMs and IONPs yielded a more significant temperature increase of 7 °C up to 41 °C (Fig. S2(b)), which resulted in an increase in the necrotic and late apoptotic cell death percentages by 10%. These *in vitro* heating behaviors are In contrast, with those observed in solution, where CMs were observed to heat much more than IONPs.

The mechanisms of cellular death induced by CMs and IONPs were further examined. CMs appear to induce cellular death mainly through early apoptosis, with a percentage of early apoptotic cell death that increased with increasing CM concentrations from 15% at 40 µg/ml to 50% at 1 mg/ml. Similar percentages were observed for CMs with/without AMF (Fig. 2(e)); this cell death mechanism was not observed with IONPs (Fig. 2(f)).

The differences in cell death mechanisms observed for IONPs and CMs as well as the more pronounced decrease in heating efficacy for CMs than IONPs observed between the *in vitro* and in suspension heating conditions may be explained by the different internalization properties. Indeed, the quantity of iron released from the nanoparticles, which are internalized in each cell, increased from 36.8 and 5.5 pg per cell without AMF application to 255.7 and 19.8 pg per cell with AMF application for the CMs and IONPs, respectively. It therefore appears that CMs are internalized better than IONPs and that the

398   internalization is enhanced by the presence of the AMF for both types of nanoparticles. This

399   enhancement is more pronounced for CMs than for IONP by factors of 7 and 4, respectively (Figure

400   2(b)). The different internalization properties for the CMs and IONPs may be explained by differences

401   in their charges, *i.e.,* CM and IONP are negatively and positively charged at physiological pH,

402   respectively (Table 1)); differences in organization, *i.e.,* CM and IONP are well-dispersed and tend to

403   aggregate, respectively; and to larger values of coercivity for CMs (200-300 Oe) compared to IONPs

404   (120 Oe) that may enhance CM magnetic field coupling. Furthermore, CM organization in chains may

405   favor internalization by groups containing several magnetosomes (30), *i.e.,* potentially 6 for chains

406   averaging 250 nm in length (Fig. S1(b), while IONPs may result in nanoparticles being internalized one

407   by one or at a lower rate. The enhanced internalization of CMs may favor early apoptosis, which was

408   previously observed with iron oxide nanoparticles, (53), and reduce its heating properties, possibly by

409   preventing nanoparticle Brownian heating mechanisms (54).

3.4. *CMs promote enhanced antitumor efficacy towards intracranial U87-Luc glioblastoma*

411   In the *in vivo* studies, mice receive the following treatment at the center of intracranial U87-Luc tumors:

412   (1) glucose followed by treatment or not with magnetic sessions (groups 1 and 2), (2) 40 µg of CMs or

413   IONPs in maghemite without any further treatment (groups 3 and 6), (3) 40 µg of CMs in maghemite

414   followed by 15 magnetic sessions (groups 4 and 5), or (4) 40 µg of IONPs in maghemite followed by 12

415   magnetic sessions (group 7). The average size of the treated tumors was 3-5 mm^3, except in group 5

416   where it was 25 mm^3. Following injection, the mice were exposed to 12 to 15 magnetic sessions, during

417   which an AMF of 198 kHz and strength 30 mT was applied for 30 minutes (see Table S1(a) for a

418   summary of the treatment conditions). In this study, U87 cells were labeled with the firefly luciferase

419   gene to evaluate the changes in tumor volumes following the treatments via tumor bioluminescence

420   intensity (BLI) measurements using the relationship between BLI and tumor volumes that we

421   established (Fig. S3) (40), (42), (43), (44). For the mice belonging to the different groups without

422   any measurable production of heat (groups 1, 2, 3, 6, and 7), Figures 3(a) to 3(e) show that the tumor

423   volumes increased following tumor cell implantation without any signs of antitumor activity. Mice

belonging to these groups were rapidly euthanized between days 28 and 42, leading to a rather low median survival time of 42 to 46 days. In contrast, in the mice belonging to groups with heated tumors (groups 4 and 5), antitumor activity is clearly observed and is more pronounced in the small (group 4) than in the large (group 5) treated tumors.
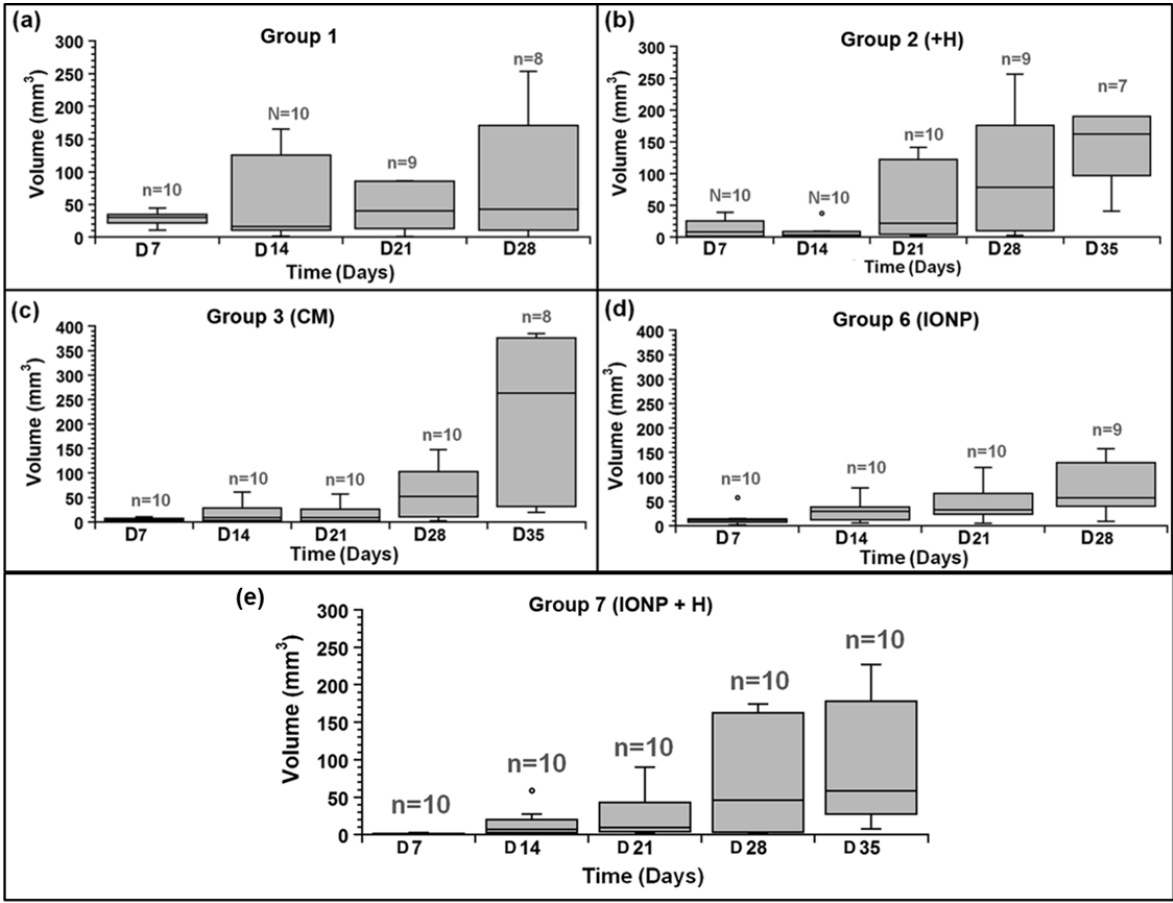
Figure 3: Variations in tumor volumes as a function of time during the days following U87-Luc tumor cell implantation at D0 for (a) untreated mice (group 1), (b) mice exposed to 15 magnetic sessions (group 2, +H), mice receiving a suspension containing either (c) 40 µg of CMs in iron oxide at the site of tumor cell implantation (group 3) or 40 µg of IONPs in iron oxide (group 6, IONP), or (e) 40 µg of IONPs in iron oxide and exposed to 15 magnetic sessions. These variations are plotted using Tukey diagrams, where error bars designate the maximum and minimum tumor volume values, circles represent single tumor values, lower and upper horizontal rectangular sides designate lower and upper quartiles, respectively, and horizontal lines within each box plot represents median tumor volumes. The number of living mice used to draw each box plot (n) is also indicated above each box plot.

Figures 4(a) shows that tumor growth is delayed in group 5 with a median tumor volume that first decreases from 25 mm^3 at day 7 to 5 mm^3 at day 14 and then increases from 5 mm^3 at day 14 to 70 mm^3 at day 42. The behavior of a typical mouse belonging to this group is shown in Figure 4(b), which shows three tumor volume oscillations (decrease followed by increase). This suggests that AMF application causes repetitive anti-tumor activity without preventing tumor regrowth after 15 magnetic sessions. This therapy led to a survival time of 49 days, which is only slightly increased compared to the unheated groups.
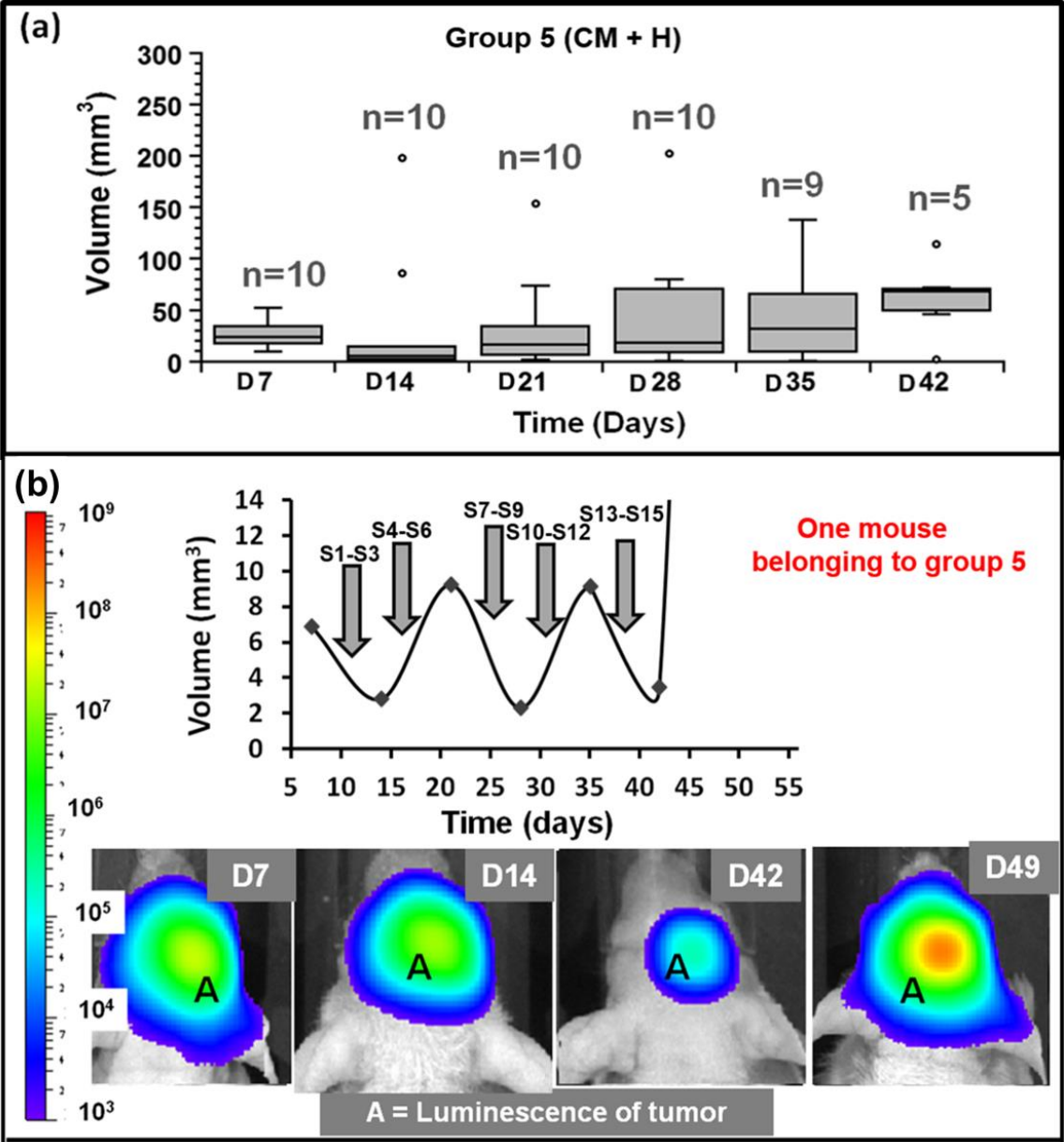
Figure 4: (a) Variations in tumor volumes as a function of time during the days following U87-Luc tumor cell implantation at

446 D0 for mice receiving a suspension containing 40 µg of CMs in iron oxide. The tumors reach an average volume of 25 mm^3

447 at D7 and were treated with 15 magnetic sessions (group 5, CM+H). (b) Variations in tumor volume and bioluminescence

448 intensity as a function of time during the days following tumor cell implantation in a mouse in group 5 with a tumor volume at

449 D7 of ~7.5 mm^3 that received 40 µg of a suspension of CMs in iron oxide on D7 followed by 15 magnetic sessions (S1 to

450 S15).

451 Figure 5(a) shows more significant antitumor activity in group 4 with full tumor disappearance at day 35

452 without tumor regrowth following 1 to 15 magnetic sessions. For a typical mouse belonging to this

453 group, Figure 5(b) shows the gradual decrease in the tumor volume following 1 to 15 magnetic sessions

454 until full tumor disappearance at day 40 without tumor regrowth. Compared with the unheated groups,

455 group 4 had the highest survival at 90 days (p-value < 0.0001).
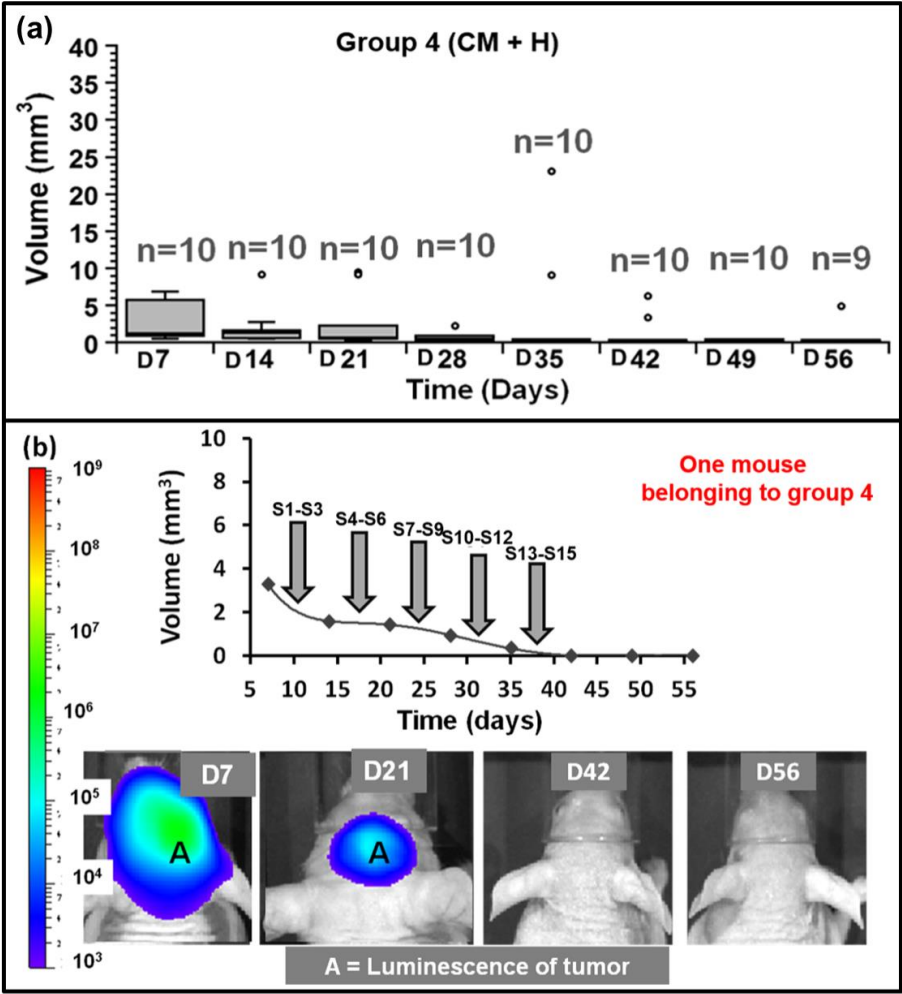

456

Figure 5: (a) Variations in tumor volumes as a function of time during the days following U87-Luc tumor cell implantation at D0 for mice receiving a suspension containing 40 µg of CMs in iron oxide when the tumors reach an average volume of 3 mm^3 at D7 followed by 15 magnetic sessions (group 4, CM+H). (b) Variations in tumor volume and bioluminescence intensity as a function of time during the days following tumor cell implantation for a mouse belonging to group 4 with a tumor volume at D7 of ~3 mm^3 that receiving 40 µg of CMs in iron oxide on D7 followed by 15 magnetic sessions (S1 to S15).

On day 150, 40% of the mice from this group were still alive without any unusual behaviors. Then, the mice were euthanized and slides of their brains from the tumor cell implantation region were imaged by optical microscopy, revealing the absence of tumors or tumor lesions and a brain neuronal structure identical to that of a healthy brain (Figure 6). These results suggest that the tumors had fully disappeared in these mice. Further analysis of mice from group 4 suggests that treatment does not result in any healthy tissue damage. Indeed, it can be deduced from the optical microscopy images of the brain sections from mice treated with CM with/without AMF collected at different times ranging from 4 hours to 150 days after CM administration (Figs. S4(a) to S4(d), S5(a) to S5(d) and Figs. 8(a) to 8(g), 9(a) to 9(d)) that healthy tissues in the hippocampus and brain do not contain lesions or edema. Such observations can be explained by an LPS-activated neuro-protective response by the microglia (55). Thus, the treatment of the mice in group 4 appears safe and fully efficient.
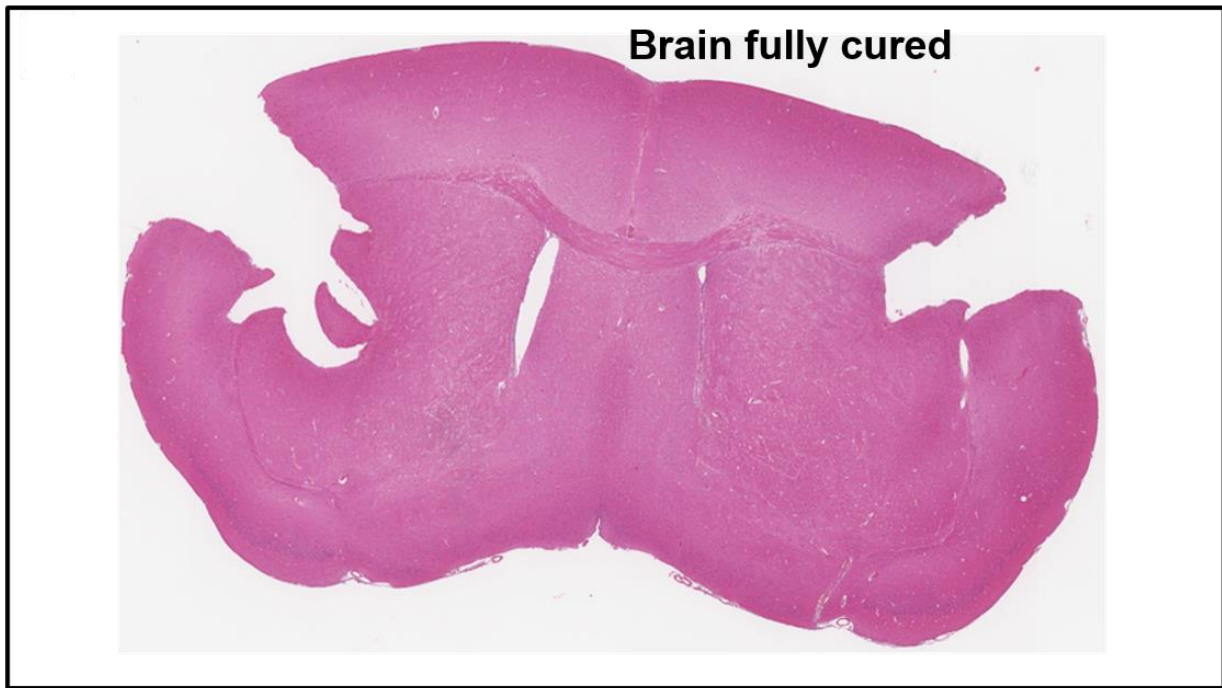
Figure 6: Optical microscopy image of a 4-µm-thick brain section stained with hematoeosin from a mouse in group 4 that received 40 µg of CMs in iron oxide followed by 15 magnetic sessions. This mouse was euthanized 7 months after magnetosome administration. No tumor was observed in this brain section.

3.5. Distribution of CMs in the tumor favors in vivo heating during the various S

CM led to temperature increases of 4 °C at D8 (S1), 1.7 °C at D9 (S2), 0.4 °C at D10, D15 and D16 (S3, S4, S5) and then constant temperatures after D17 (Figures. 7(a) and 7(b)).
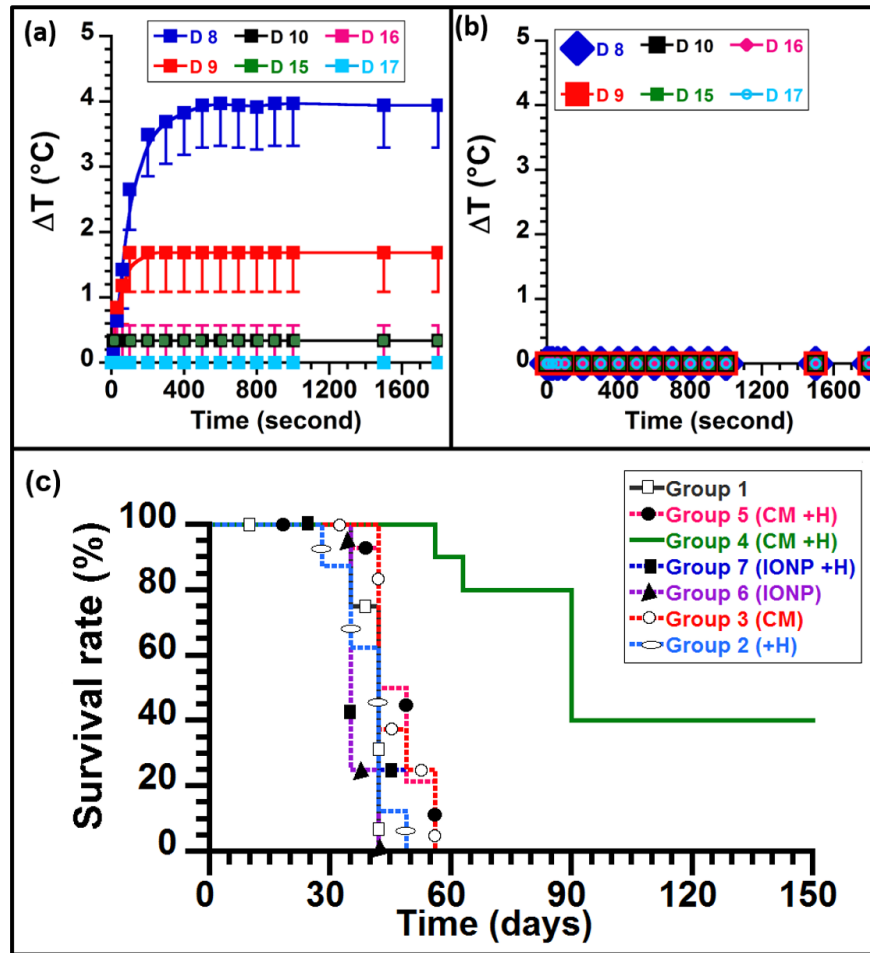
Figure 7: (a), Temperature increases above 28.5 °C observed during each magnetic session (ΔT) on D8, D9, D10, D15, D16 and D17 in the mice from groups 4 and 5 treated with CMs. (b) The same as in (a) for the mice in group 7 treated with IONPs. After D17, tumor temperature increases were no longer observed. (c)Variations in mouse survival times as a function of time during the days following U87-Luc tumor cell implantation for mice with the following treatments: (1) untreated (group 1), (2) exposed to 15 magnetic sessions (group 2), (3) treated with suspensions containing 40 µg of CMs in iron oxide without magnetic sessions (group 3), (4) treated with 40 µg of CMs in iron oxide in ~3 mm^3 tumors followed by 15 magnetic sessions (group 4), (5) administered 40 µg of CMs in iron oxide in ~25 mm^3 tumors followed by 15 magnetic sessions (group 5), (6) administered 40 µg of IONPs in iron oxide (group 6), and administered 40 µg of IONPs in iron oxide followed by 15 magnetic sessions (group 7).

The rather limited increases in temperature under AMF, which are less pronounced than in the capillaries (Fig. S2(a)), may be explained by the effects of AMF on CM distribution. Indeed, the tumor occupation percentage decreases from ~50% right after CM administration without AMF at D8 (Figs. 9(a) and 9(b)) down to 8-15% on D8 and D11 after 1 and 3 magnetic sessions, respectively, (Figs. 8(a),

24

8(b) and 8(d)). There percentages were estimated by delineating the regions containing the CMs and the tumors and by measuring the ratio between the surfaces of these two regions. Moreover, the decrease in CM heating properties over time may be attributed to internalization of CMs in U87 tumor cells, which was observed at 24 hours after 3 magnetic sessions (Fig 8(d) and 8(e)).

Figure 8: Optical microscopy images of 4 µm thick brain sections stained with hematoeosin from mice receiving 40 µg of CMs in iron oxide and exposed to (a-c) one or (d-g) three magnetic sessions. The mice were euthanized (a) 0 hours (0 h), (b and c) 4 hours (4 h), or (d-g) 72 hours (72 h) after MC administration with either (a-c) one or (d-g) three magnetic sessions. (c) An enlargement of the region in (b). The red arrows in (c) designate polynuclear neutrophils. (e), (f), and (g) are enlargements of three different regions from (d). PNN, M-PNN, U87-Luc, M-PNN & U87-Luc, and U87-Luc & magnetosomes designate polynuclear neutrophils, magnetosomes colocalized with polynuclear neutrophils, U87-Luc cells, magnetosomes colocalized with polynuclear neutrophils and U87-Luc cells, and U87-Luc cells colocalized with magnetosomes, respectively. The regions containing these different cells are surrounded in (d), while individual cells are indicated by arrows in (c), (e) and (f).

In contrast with CMs, IONPs do not produce any heat *in vivo* under the same excitation conditions. This behavior can be explained by their lower concentration in the tumor under AMF applications, *i.e.,* they are observed at the tumor surface as well as part of the tumor periphery at 6 hours (Figs. S4(a) and S4(c)); their more rapid diffusion in the ventricles, *i.e.,* IONPs and CMs localize in the ventricles at 6 and 72 hours, respectively, (Figs. S4(a) and S4(b), Figs. 8(d)); and their earlier internalization in tumor U87-Luc and healthy BETZ brain cells, *i.e.,* IONPs and CMs are internalized at 6 and 72 hours, respectively, (Figs. S4(c) and S4(d), Fig. 8(e)). The combination of a low concentration in the tumor together with rather low SAR may undermine the IONPs' heating power, as was observed *in vivo*.

3.6. CM exposed to AMF activate PNN, which are possibly involved in antitumor activities

Previous studies have reported that immune cells, such as dendritic cells, natural killers, and B and T cells, may participate in tumor destruction following hyperthermia treatment (56). Here, we examined potential involvement of other types of immune cells, *i.e.,* polynuclear neutrophils (PNN), which have only rarely been associated with antitumor activities (57), (58). While PNNs were not detected after glucose (Fig. S5) or IONP (Fig. S4) administration with/without magnetic sessions, we observed that these cells were localized at the same sites as the magnetosomes, forming a complex designated M-PNN in the mouse euthanized 4 hours after CM administration with/without magnetic sessions (Figs. 8(b), 8(c), 8(d), 8(f), 8(g), 9(a) and 9(c)). More precisely, M-PNNs designate assemblies of magnetosomes and PNNs where the magnetosomes are less than 1 μm away from the PNNs. The number of M-PNNs was estimated as 14000-19000 per mm^2 4 hours after CM administration (Table S2). Because PNNs are known to be recruited by endotoxins (59), this behavior could be attributed to the endotoxins surrounding the magnetosome mineral core that attract PNN. Seventy-two hours later, the M-PNNs had disappeared in the absence of AMF (Figs. 9(b) and 9(d) and Table S2) but were detected in large quantities of 27,500 per mm^2 (Table S2) after 3 magnetic sessions either within the tumor periphery (Fig. 8(d) and 8(f)) or in the tumor (Figs. 8(d) and 8(e)).
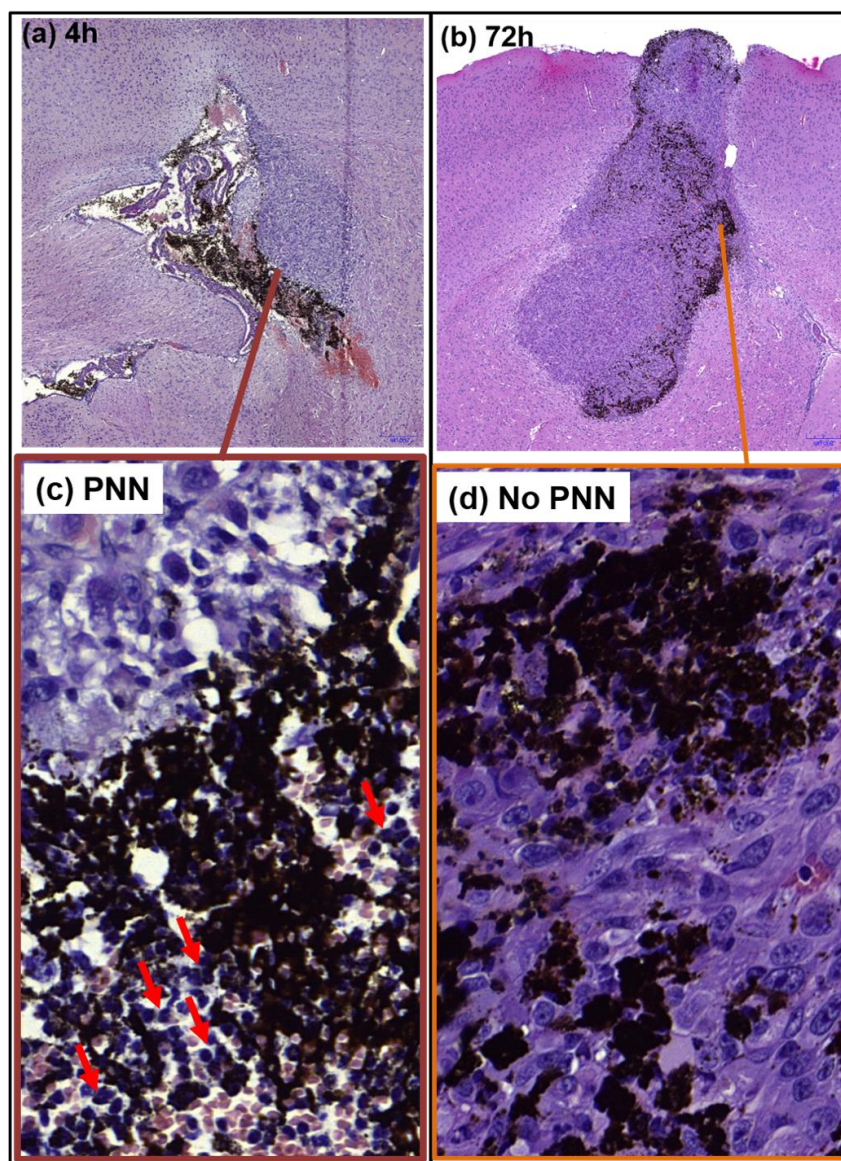
Figure 9: Optical microscopy images of 4 µm thick brain sections stained with hematoeosin from mice receiving 40 µg of CMs in iron oxide without magnetic sessions and euthanized (a) 4 hours (4 h) or (b) 72 hours (72 h) after magnetosome administration. (c) and (d) are enlargements of two regions in (a) and (b), respectively. PNN are observed in (c) and indicated by red arrows, but not in (d).

These interesting behaviors might suggest that in the absence of AMF, endotoxins are progressively deactivated, perhaps due to magnetosome internalization followed by magnetosome and endotoxin decomposition. However, in the presence of AMF, the endotoxins are re-activated, possibly through the release of endotoxins from the magnetosome surface, a behavior that perfectly fits with the observations in solution (Fig. 2(a)) and/or via the destruction of cells in which magnetosomes are initially internalized before AMF application. M-PNN complexes may have two main functions. First, they may be involved

27

545   in tumor destruction, as they are observed in the tumor region and Toll-like receptor (TLR) from the

546   treated mice could be activated and trigger antitumor activity; this was previously reported for mice

547   bearing B16 tumors (60). Second, they may also be involved in magnetosome capture and re-

548   distribution. Indeed, after one and three magnetic sessions, magnetosomes and PNNs alone are rarely

549   observed in the entire brain, including the tumor regions (Figs. 7(b) and 7(d)), and M-PNNs appear to be

550   located either in the tumor, near the tumor periphery or in the ventricles (Figs. 7(b) and 7(c)). These

551   results suggest that PNNs progressively migrate in the region where the magnetosomes are located

552   between 0 and 4 hours after CM administration to form M-PNN complexes and that these complexes

553   carry the magnetosomes from the inside to the outside of the tumor, possibly through the ventricle blood

554   vessels. This behavior further agrees with the absence of heat production after D17, which suggests that

555   magnetosomes have left the tumor by this date and/or have been dissolved into free iron. This idea is

556   also in line with the well-known function of PNNs, which is to remove bacterial residues (61), (62).

557   Magnetosome progressive departure from the tumor, possibly followed by magnetosome redistribution

558   within the mouse, could be appealing for the treatment by preventing crystallized magnetosomes from

559   remain in the brain for too long a period of time. Optimum treatment conditions correspond to those

560   where magnetosomes remain in the brain long enough to perform the treatment, but not for too long, to

561   avoid unnecessary long-term magnetosome interactions with brain tissues. These conditions may be

562   identified by controlling PNN activation and M-PNN complex formation under AMF application.

563   *3.7. CMs appear to destroy glioblastoma tumors more efficiently than chemically synthesized*

564   *nanoparticles under AMF applications*

565   Using the same quantity of nanoparticles administered, we have shown in this study that CMs lead to

566   40% of mice with full tumor disappearance, while IONPs do not yield any observable antitumor

567   activities. This result agrees with previous animal studies performed on mice and rats bearing GBM

568   using intratumor administration of chemically synthesized nanoparticles exposed to AMF that did not

569   improve survival (63) or increased survival by 15 days without resulting in a full cure (64), (26). In

570   addition to being more efficient, magnetosomes could also be used in a lower quantity, thus

strengthening treatment safety. Indeed, the quantity of magnetosomes necessary to eradicate U87-Luc GBM in this study, which was 1 to 13 μg in maghemite per mm^3 of tumor volume, is much less than 60 μg per mm^3 of tumor volume, which produced less-efficient anti-tumor activities with chemically synthesized nanoparticles (9).

4. CONCLUSION

We demonstrated that 40% of mice bearing intracranial U87-Luc tumors displayed full tumor disappearance after intratumor administration of 40 μg of CMs followed by 12 to 15 magnetic sessions, during which an AMF of average strength 30 mT and frequency 198 kHz was applied for 30 minutes. In contrast, similar antitumor efficacy was not observed when mice were treated with the same conditions and administered chemically synthesized nanoparticles instead of magnetosomes. Furthermore, the absence of mouse brain damage during and following the various treatments appears to indicate that a safe treatment could be performed with magnetosomes, provided that the endotoxins are replaced with an equivalently active but nonpyrogenic substance such as M-PLA. Antitumor activity does not appear to be dominated by nanoparticle cytotoxicity, as the CMs, which are more efficient than IONPs *in vivo*, do not enhance cytotoxicity towards U87-Luc cells compared with IONPs. Moreover, nanoparticle administration without AMF does not produce any observable anti-tumor effects. Instead, tumor destruction appears to be due to the heat produced by the CMs under AMF application, as the only mice that displayed clear anti-tumor effects had their tumors heated (groups 4 and 5). Under heating conditions, tumor tissue destruction may be caused by irreversible cell damage; cytolysis; actin filament, microtubule or mitochondrial dysfunction; DNA replication or RNA synthesis inhibition; or DNA polymerase denaturation (65), but these mechanisms seem insufficient to fully explain the observed antitumor activities. Indeed, tumor destruction does occur when the magnetosomes occupy a small percentage of the total tumor volume (~10%), suggesting that magnetosomes occupying the tumor can induce the destruction of the entire tumor. We have identified the following three possible mechanisms that could be responsible for full tumor destruction:

596 i) Early apoptosis, as apoptotic cell death is observed to be dominant *in vitro* for CMs and heat was

597 previously shown to favor apoptotic cell death (65), (66), (67);

598 ii) Microvascular damage due to the presence of magnetosomes in the ventricles that possibly leads

599 to the destruction of the blood vessels supplying the tumor with oxygen, which was previously reported

600 to occur during hyperthermia, (68), and could possibly occur because CMs were observed in the

601 ventricles near the blood vessel; and

602 iii) the involvement of PNN, which were previously reported to be involved in antitumor activity,

603 (58) and were attracted by the magnetosomes in the tumor region due to the presence of endotoxins at

604 magnetosome surface.

605 Finally, our study also suggests a method to control magnetosome distribution by attracting PNNs to the

606 magnetosome region, which promotes the formation of magnetosome/PNN complexes that may

607 progressively remove magnetosomes from the tumor through the ventricle blood vessels and enable their

608 elimination. This process appears to be governed by the application (or not) of an AMF.

615 *Abbreviations*

616 GBM   glioblastoma
617 AMF   alternating magnetic field
618 IONP   iron oxide nanoparticles
619 CM   magnetosome chains

620	UV	irradiation of an ultraviolet lamp
621	LAL	limulus amebocyte lysate
622	DMEM	Dulbecco's Modified Eagle Medium
623	FBS	fetal bovine serum
624	HBSS	Hank's Balanced Salt Solution
625	S	magnetic sessions
626	BLI	bioluminescence intensity
627	H&E	hematoxylin-eosin
628	PNN	polynuclear neutrophils
629	SAR	specific absorption rates
630	TLR	toll like receptor
631	M-PNN	PNN were localized at the same site as magnetosomes

632 **REFERENCES**

633 1. E. Alphandéry, P. Grand-Dewyse, R. Lefèvre, C. Mandawala, M. Durand-Dubief, Cancer
634 therapy using nanoformulated substances: scientific, regulatory and financial aspects. Expert Review of
635 Anticancer Therapy. 15 (2015) 1233–55.

636 2. D.P. O'Neal, L.R. Hirsch, N.J. Halas, J.D. Payne, J.L. West, Photo-thermal tumor ablation in
637 mice using near infrared-absorbing nanoparticles. Cancer Letters. 209 (2004) 171–6.

638 3. I.H. El-Sayed, X. Huang, M.A. El-Sayed, Selective laser photo-thermal therapy of epithelial
639 carcinoma using anti-EGFR antibody conjugated gold nanoparticles. Cancer Lett. 239 (2006) 129–35.

640 4. X.Y. Su, P.D. Liu, H. Wu, N. Gu, Enhancement of radiosensitization by metal-based
641 nanoparticles in cancer radiation therapy. Cancer Biol Med. 11 (2014) 86–91.

642 5. S. Her, D.A. Jaffray, C. Allen, Gold nanoparticles for applications in cancer radiotherapy:
643 Mechanisms and recent advancements. Advanced Drug Delivery Reviews. (2015) *in Press*
644 http://dx.doi.org/10.1016/j.addr.2015.12.012.

645   6.   O.K. Kosheleva, T.C. Lai, N.G. Chen, M. Hsiao, C.H. Chen, Selective killing of cancer cells by

646   nanoparticle-assisted ultrasound. Journal of Nanobiotechnology. (2016) 14:46.

647   7.   Y. You, Z. Wang, H. Ran, Y. Zheng, D. Wang, J. Xu, and al, Nanoparticle-enhanced synergistic

648   HIFU ablation and transarterial chemoembolization for efficient cancer therapy. Nanoscale 8 (2016)

649   4324–39.

650   8.   M. Bañobre-López, A. Teijeiro, J. Rivas, Magnetic nanoparticle-based hyperthermia for cancer

651   treatment. Reports of Practical Oncology & Radiotherapy 18 (2013) 397-400.

652   9.   A. Jordan, R. Scholz, K. Maier-Hauff, F.K.H.V. Landeghem, N. Waldoefner, U. Teichgraeber,

653   and al, The effect of thermotherapy using magnetic nanoparticles on rat malignant glioma. J

654   Neurooncol. 78 (2005) 7-14.

655   10.   J.A. Schwartzbaum, J.L. Fisher, K.D. Aldape, M. Wrensch, Epidemiology and molecular

656   pathology of glioma. Nature Clinical Practice Neurology 2 (2006) 494–503.

657   11.   UK CR. Types of primary brain tumors. Last accessed 13 August 2009 at

658   http://www.cancerhelp.org.uk/help/default.asp?page=5014

659   12.   Q.T. Ostrom, L. Bauchet, F.G. Davis, I. Deltour, J.L. Fisher, C.E. Langer, and al, The

660   epidemiology of glioma in adults: a "state of the science" review. Neuro Oncol. 16 (2014) 896–913.

661   13.   R. Stupp, M.E. Hegi, W.P. Mason, M.J. van den Bent, M.J. Taphoorn, R.C. Janzer, and al,

662   Effects of radiotherapy with concomitant and adjuvant temozolomide versus radiotherapy alone on

663   survival in glioblastoma in a randomised phase III study: 5-year analysis of the EORTC-NCIC trial. The

664   Lancet Oncology 10 (2009) 459–66.

665   14.   C. Billecke, S. Finniss, L. Tahash, C. Miller, T. Mikkelsen, N.P. Farrell, and al., Polynuclear

666   platinum anticancer drugs are more potent than cisplatin and induce cell cycle arrest in glioma. Neuro-

667   oncol 8 (2006) 215–26.

668   15.   H.H. Ross, M. Rahman, L.H. Levkoff, S. Millette, T. Martin-Carreras, E.M. Dunbar, and al.,

669   Ethynyldeoxyuridine (EdU) suppresses in vitro population expansion and in vivo tumor progression of

670   human glioblastoma cells. J Neurooncol. 105 (2011) 485–98.

671   16.   F-Y. Yang, M-C. Teng, M. Lu, H-F. Liang, Y-R. Lee, C-C. Yen, and al., Treating glioblastoma

672   multiforme with selective high-dose liposomal doxorubicin chemotherapy induced by repeated focused

673   ultrasound. Int J Nanomedicine 7(2012) 965–74.

674   17.   F. Safdie, S. Brandhorst, M. Wei, W. Wang, C. Lee, S. Hwang, and al., Fasting Enhances the

675   Response of Glioma to Chemo- and Radiotherapy. PLOS ONE 7 (2012) e44603.

676   18.   G.L. Bidwell, E. Perkins, J. Hughes, M. Khan, J.R. James, D. Raucher, Thermally Targeted

677   Delivery of a c-Myc Inhibitory Polypeptide Inhibits Tumor Progression and Extends Survival in a Rat

678   Glioma Model. PLOS ONE 8. (2013) e55104.

679   19.   W.L. Titsworth, G.J.A. Murad, B.L. Hoh, M. Rahman, Fighting Fire with Fire: The Revival of

680   Thermotherapy for Gliomas. Anticancer Res. 34 (2014) 565–74.

681   20.   F. Jiang, X. Zhang, S.N. Kalkanis, Z. Zhang, H. Yang, M. Katakowski, and al., Combination

682   Therapy with Antiangiogenic Treatment and Photodynamic Therapy for the Nude Mouse Bearing U87

683   Glioblastoma. Photochem Photobiol. 84 (2008) 128–37.

684   21.   I. Rabias, D. Tsitrouli, E. Karakosta, T. Kehagias, G. Diamantopoulos, M. Fardis, and al., Rapid

685   magnetic heating treatment by highly charged maghemite nanoparticles on Wistar rats exocranial glioma

686   tumors at microliter volume. Biomicrofluidics. 4 (2010) 024111.

687   22.   M. Shinkai, M. Yanase, M. Suzuki, H. Honda, T. Wakabayashi, J. Yoshida, and al., Intracellular

688   hyperthermia for cancer using magnetite cationic liposomes. Journal of Magnetism and Magnetic

689   Materials. 194 (1999) 176–84.

23.   A. Ito, M. Shinkai, H. Honda, T. Kobayashi, Heat-inducible TNF-alpha gene therapy combined with hyperthermia using magnetic nanoparticles as a novel tumor-targeted therapy. Cancer Gene Ther. 8 (2001) 649–54.

24.   T. Ohno, T. Wakabayashi, A. Takemura, J. Yoshida, A. Ito, M. Shinkai, and al., Effective Solitary Hyperthermia Treatment of Malignant Glioma Using Stick Type CMC-magnetite. In vivo Study. J Neurooncol. 56 (2002) 233–9.

25.   B. Le, M. Shinkai, T. Kitade, H. Honda, J. Yoshida, T. Wakabayashi, and al., Preparation of Tumor-Specific Magnetoliposomes and Their Application for Hyperthermia. Journal of Chemical Engineering of Japan. 34 (2001) 66–72.

26.   K. Maier-Hauff, R. Rothe, R. Scholz, U. Gneveckow, P. Wust, B. Thiesen, and al., Intracranial thermotherapy using magnetic nanoparticles combined with external beam radiotherapy: results of a feasibility study on patients with glioblastoma multiforme. J Neurooncol. 81 (2007) 53–60.

27.   K. Maier-Hauff, F. Ulrich, D. Nestler, H. Niehoff, P. Wust, B. Thiesen, and al., Efficacy and safety of intratumoral thermotherapy using magnetic iron-oxide nanoparticles combined with external beam radiotherapy on patients with recurrent glioblastoma multiforme. J Neurooncol. 103 (2011) 317–24.

28.   E. Alphandéry, S. Faure, O. Seksek, F. Guyot, I. Chebbi, Chains of Magnetosomes Extracted from AMB-1 Magnetotactic Bacteria for Application in Alternative Magnetic Field Cancer Therapy. ACS Nano. 5 (2011) 6279–96.

29.   E. Alphandéry, F. Guyot, I. Chebbi, Preparation of chains of magnetosomes, isolated from Magnetospirillum magneticum strain AMB-1 magnetotactic bacteria, yielding efficient treatment of tumors using magnetic hyperthermia. International Journal of Pharmaceutics. 434 (2012) 444–52.

712   30.   E. Alphandéry, M. Amor, F. Guyot, I. Chebbi, The effect of iron-chelating agents on
713   Magnetospirillum magneticum strain AMB-1: Stimulated growth and magnetosome production and
714   improved magnetosome heating properties. Applied Microbiology and Biotechnology. 96 663–70.

715   31.   E. Alphandéry, S. Faure, L. Raison, E. Duguet, P.A. Howse, D.A. Bazylinski, Heat Production
716   by Bacterial Magnetosomes Exposed to an Oscillating Magnetic Field. J Phys Chem C. 115 (2011) 18–
717   22.

718   32.   E. Alphandéry, I. Chebbi, F. Guyot, M. Durand-Dubief, Use of bacterial magnetosomes in the
719   magnetic hyperthermia treatment of tumours: A review. International Journal of Hyperthermia. 29
720   (2013) 801–9.

721   33.   E. Alphandéry, Applications of Magnetosomes Synthesized by Magnetotactic Bacteria in
722   Medicine. Front Bioeng Biotechnol. 11 (2014) 2:5.

723   34.   D.E. Bordelon, C. Cornejo, C. Grüttner, F. Westphal, T.L. DeWeese, R. Ivkov, Magnetic
724   nanoparticle heating efficiency reveals magneto-structural differences when characterized with wide
725   ranging and high amplitude alternating magnetic fields. Journal of Applied Physics. 109 (2011) 124904.

726   35.   C. Grüttner, K. Müller, J. Teller, F. Westphal, A. Foreman, R. Ivkov, Synthesis and antibody
727   conjugation of magnetic nanoparticles with improved specific power absorption rates for alternating
728   magnetic field cancer therapy. Journal of Magnetism and Magnetic Materials. 311 (2007) 181–6.

729   36.   K. Cui, X. Xu, H. Zhao, S.T.C. Wong, A quantitative study of factors affecting in vivo
730   bioluminescence imaging. Luminescence. 23 (2008) 292–5.

731   37.   A. Sun, L. Hou, T. Prugpichailers, J. Dunkel, M.A. Kalani, X. Chen, and al., Firefly luciferase-
732   based dynamic bioluminescence imaging: a noninvasive technique to assess tumor angiogenesis.
733   Neurosurgery. 66 (2010) 751–757.

734 38.   R. Hashizume, T. Ozawa, E.B. Dinca, A. Banerjee, M.D. Prados, C.D. James, and al., A human

735   brainstem glioma xenograft model enabled for bioluminescence imaging. J Neurooncol. 96 (2010) 151–

736   9.

737 39.   E.B. Dinca, J.N. Sarkaria, M.A. Schroeder, B.L. Carlson, R. Voicu, N. Gupta, and al.,

738   Bioluminescence monitoring of intracranial glioblastoma xenograft: response to primary and salvage

739   temozolomide therapy. J Neurosurg. 107 (2007) 610–6.

740 40.   O. Szentirmai, C.H. Baker, N. Lin, S. Szucs, M. Takahashi, S. Kiryu, and al., Noninvasive

741   Bioluminescence Imaging of Luciferase Expressing Intracranial U87 Xenografts: Correlation with

742   Magnetic Resonance Imaging Determined Tumor Volume and Longitudinal Use in Assessing Tumor

743   Growth and Antiangiogenic Treatment Effect. Neurosurgery. 58 (2006) 365-372.

744 41.   H. Zhou, K. Luby-Phelps, B.E. Mickey, A.A. Habib, R.P. Mason, D. Zhao, Dynamic Near-

745   Infrared Optical Imaging of 2-Deoxyglucose Uptake by Intracranial Glioma of Athymic Mice. PLOS

746   ONE. 4 (2009) e8051.

747 42.   D.F. Heitjan, A. Manni, R.J. Santen, Statistical analysis of in vivo tumor growth experiments.

748   Cancer Res. 53 (1993) 6042–50.

749 43.   S-J. Kim, H.J. Lee, M.S. Kim, H.J. Choi, J. He, Q. Wu, et al., Macitentan, a Dual Endothelin

750   Receptor Antagonist, in Combination with Temozolomide Leads to Glioblastoma Regression and Long-

751   term Survival in Mice. Clin Cancer Res. 21 (2015) 4630–41.

752 44.   E. Alphandéry, A.T. Ngo, C. Lefèvre, I. Lisiecki, L.F. Wu, M.P. Pileni. Difference between the

753   Magnetic Properties of the Magnetotactic Bacteria and Those of the Extracted Magnetosomes: Influence

754   of the Distance between the Chains of Magnetosomes. J Phys Chem C. 112 (2008) 12304–9.

755 45.   D.A. Bazylinski, R.B. Frankel, Magnetosome formation in prokaryotes. Nat Rev Micro. 2 (2004)

756   217–30.

757 46. L.C. Branquinho, M.S. Carrião, A.S. Costa, N. Zufelato, M.H. Sousa, R. Miotto, and al., Effect

758 of magnetic dipolar interactions on nanoparticle heating efficiency: Implications for cancer

759 hyperthermia. Scientific Reports. 3 (2013) 2887.

760 47. C. Grüttner, K. Müller, J. Teller, F. Westphal, A. Foreman, R. Ivkov, Synthesis and antibody

761 conjugation of magnetic nanoparticles with improved specific power absorption rates for alternating

762 magnetic field cancer therapy. Journal of Magnetism and Magnetic Materials. 311 (2007) 181–6.

763 48. C.R. Casella, T.C. Mitchell, Putting endotoxin to work for us: monophosphoryl lipid A as a safe

764 and effective vaccine adjuvant. Cell Mol Life Sci. 65 (2008) 3231–40.

765 49. M.E. Astiz, E.C. Rackow, J.G. Still, S.T. Howell, A. Cato, K.B. Von Eschen, and al.,

766 Pretreatment of normal humans with monophosphoryl lipid A induces tolerance to endotoxin: a

767 prospective, double-blind, randomized, controlled trial. Crit Care Med. 23 (1995) 9–17.

768 50. Y. Liu, J. Wang, Effects of DMSA-Coated Fe3O4 Nanoparticles on the Transcription of Genes

769 Related to Iron and Osmosis Homeostasis. Toxicol Sci. 131 (2013) 521–36.

770 51. A. Tomitaka, Y. Takemura, Measurement of Specific Loss Power from Intracellular Magnetic

771 Nanoparticles for Hyperthermia. J Personali NanoMedicine. 1 (2015) 33-37.

772 52. D.A. Bazylinski, R.B. Frankel, Magnetosome formation in prokaryotes. Nat Rev Micro. 2 (2004)

773 217–30.

774 53. M. Creixell, A.C. Bohórquez, M. Torres-Lugo, C. Rinaldi, EGFR-Targeted Magnetic

775 Nanoparticle Heaters Kill Cancer Cells without a Perceptible Temperature Rise. ACS Nano. 5 (2011)

776 7124–9.

777 54. Z. Chen, W. Jalabi, K.B. Shpargel, K.T. Farabaugh, R. Dutta, X. Yin, and al.,

778 Lipopolysaccharide-Induced Microglial Activation and Neuroprotection against Experimental Brain

779 Injury Is Independent of Hematogenous TLR4. J Neurosci. 32 (2012) 11706–15.

780 55. T. Mentzel, L.F. Brown, H.F. Dvorak, C. Kuhnen, K.J. Stiller, D. Katenkamp, and al., The

781 association between tumor progression and vascularity in myxofibrosarcoma and myxoid/round cell

782 liposarcoma. Virchows Arch. 438 (2001) 13–22.

783 56. L. Asín, G.F. Goya, A. Tres, M.R. Ibarra, Induced cell toxicity originates dendritic cell death

784 following magnetic hyperthermia treatment. Cell Death Dis. 4 (2013) e596.

785 57. F. Eriksson, P. Tsagozis, K. Lundberg, R. Parsa, S.M. Mangsbo, M.A.A. Persson, and al.,

786 Tumor-Specific Bacteriophages Induce Tumor Destruction through Activation of Tumor-Associated

787 Macrophages. J Immunol. 182 (2009) 3105–11.

788 58. J. Liang, Y. Piao, L. Holmes, G.N. Fuller, V. Henry, N. Tiao, and al., Neutrophils Promote the

789 Malignant Glioma Phenotype through S100A4. Clinical Cancer Research. 20 (2014) 187–98.

790 59. A.W. Segal, How Neutrophils Kill Microbes. Annu Rev Immunol. 23 (2005) 197–223.

791 60. A.C. Silva, T.R. Oliveira, J.B. Mamani, S.M. Malheiros, L. Malavolta, L.F. Pavon, and al.,

792 Application of hyperthermia induced by superparamagnetic iron oxide nanoparticles in glioma

793 treatment. Int J Nanomedicine. 6 (2011) 591–603.

794 61. A. Jordan, R. Scholz, K. Maier-Hauff, F.K.H.V. Landeghem, N. Waldoefner, U. Teichgraeber,

795 and al., The effect of thermotherapy using magnetic nanoparticles on rat malignant glioma. J

796 Neurooncol. 78 (2006) 7–14.

797 62. K.F. Chu, D.E. Dupuy, Thermal ablation of tumours: biological mechanisms and advances in

798 therapy. Nat Rev Cancer. 14 (2014) 199–208.

799 63. D.C. Wang, Y. Zhang, H.Y. Chen, X.L. Li, L.J. Qin, Y.J. Li, H.Y. Zhang, S. Wang,

800 Hyperthermia Promotes Apoptosis and Suppresses Invasion in C6 Rat Glioma Cells. Asian Pacific

801 Journal of Cancer Prevention. 13 (2012) 3239–45.

802   64.   A. Morlé, C. Garrido, O. Micheau, Hyperthermia restores apoptosis induced by death receptors

803   through aggregation-induced c-FLIP cytosolic depletion. Cell Death Dis. 6 (2015) e1633.

804   65.   M. Nikfarjam, V. Muralidharan, C. Christophi, Mechanisms of Focal Heat Destruction of Liver

805   Tumors. Journal of Surgical Research. 127 (2005) 208–23.

806